Journal of Industrial and Engineering Chemistry 51 (2017) 196–205

Contents lists available at ScienceDirect

Journal of Industrial and Engineering Chemistry

journal homepage: www.elsevier.com/locate/jiec

Catalytic conversion of syngas to higher alcohols over mesoporous perovskite catalysts

Tae-Wan Kim[a,c,*], Freddy Kleitz[b], Jong Won Jun[a], Ho-Jeong Ch[a,c], Chul-Ung Kim[a,c]

[a] Center for Convergent Chemical Process, Korea Research Institute of Chemical Technology, 141, Gajeong-ro, Yuseong-gu, Daejeon 34114, South Korea
[b] Institute of Inorganic Chemistry—Functional Materials, University of Vienna, Währinger Straβe 42, 1090 Vienna, Austria
[c] Department of Advanced Materials and Chemical Engineering, University of Science and Technology (UST), 217 Gajeong-Ro, Daejeon 305-350, Yuseong, South Korea

ARTICLE INFO

Article history:
Received 18 November 2016
Received in revised form 25 February 2017
Accepted 27 February 2017
Available online 9 March 2017

Keywords:
Mesoporous material
Mixed alcohols
Syngas to alcohols
Nanocast
Perovskites

ABSTRACT

Two types of mesoporous perovskite-type oxides (Meso-PTOs) were synthesized by combining a templated synthesis and a citrate complex method. The Meso-PTO catalysts exhibited superior catalytic activity in the higher alcohols synthesis from syngas compared to the bulk-PTO, likely due to the increased dispersion of active sites on the high surface of the Meso-PTOs. Moreover, the Meso-PTOs show higher productivity for C_3 and C_4 alcohols as well as C_{2+} oxygenates. Among the two Meso-PTOs developed here, the mesoporous $LaFe_{0.7}Cu_{0.3}O_3$ catalyst was capable of significant suppression of the methanation reaction and better selectivity to higher alcohols compared to the mesoporous $LaCo_{0.7}Cu_{0.3}O_3$ catalyst.

Introduction

C_{2+} alcohols (higher alcohols) have attracted interest regarding their use as alternative fuels, fuel additives, energy carriers, and basic chemical intermediates and feedstocks [1–3]. Typically, ethanol is produced by the fermentation of edible resources, and propanol and butanol are obtained from petroleum-derived light olefins. At present, given the unstable oil prices, the depletion of oil resources, and the necessity to reduce greenhouse gases, the demand for alternative routes by which to realize the production of higher alcohols from renewable, non-edible, and non-petroleum resources such as biomass, natural gas, and coal, is growing. In addition, the recent growth in the non-conventional natural gas (shale gas) industry has brought about increased interest in the catalytic thermochemical conversion of syngas to higher alcohols (STA) coupled with the reforming of natural gas to syngas.

Over the past few decades, many researchers have studied the STA reaction which occurs via a catalytic thermochemical route using various catalysts. A typical STA catalyst from the noble metal group is the Rh-based catalyst, which is well known to produce ethanol and C_2 oxygenates selectively [4–8]. However, a high Rh amount (>4–5 wt%) and the high price of this precious metal have prevented its application and commercialization [9–12]. Therefore, many other studies have attempted to carry out the STA reaction using non-noble-metal catalysts for more economically viable applications and commercialization. The non-noble-metal catalysts for the STA reaction are mainly divided into three modified-catalytic systems: methanol synthesis [2,13–15], the Fischer–Tropsch (FT) process [16–20], and hydrodesulfurization catalysts [13,21,22]. Among these non-noble-metal catalysts, copper-modified FT catalysts (e.g., Co–Cu and Fe–Cu-based catalysts) have been considered as good candidates as STA catalysts given their higher alcohol selectivity levels [3,23]. In Cu-modified FT catalysts, the formation of higher alcohol can be expected due to the synergetic effect of both Cu and FT elements (e.g., Co and Fe). FT elements serve as active sites to dissociate CO forming a surface metal-alkyl bond, whereas the Cu element influences alcohol formation by facilitating the insertion of CO into the metal-alkyl bond [24,25].

Perovskite-type oxides (PTOs) have been used in a wide range of applications as catalysts owing to their high catalytic activity, good thermal stability, and low cost [26]. In particular, PTOs have been used as FT and STA catalysts for the conversion of syngas to many useful chemicals and liquid fuels owing to the uniformly distributed active metal ion species at the atomic level in the spinel structure [26–37]. Kaliaguine and coworkers extensively studied Co–Cu-based perovskites ($LaCo_{1-x}Cu_xO_{3-\delta}$, denoted as GM) prepared by reactive grinding for the production of mixed alcohols [32–35]. More recently, Liu's group proposed a catalyst

* Corresponding author. Fax: +82 42 860 7508.
E-mail address: twkim@krict.re.kr (T.-W. Kim).

http://dx.doi.org/10.1016/j.jiec.2017.02.032
1226-086X/

based on highly dispersed Co_3O_4 supported on $LaFe_{0.7}Cu_{0.3}O_3$ for higher alcohol synthesis from syngas [30]. However, perovskites prepared by conventional synthetic methods still have low specific surface areas ($<10\,m^2/g$) and poorly developed porosity, which limit their efficiency in potential applications. Thus, many synthetic routes have been proposed to increase the specific surface area of PTOs by solid-state reactions, coprecipitation, freeze drying, flame-hydrolysis, sol–gel processes (e.g., the citric complex method), and reactive grinding [35,38–41]. However, the resultant PTOs still presented rather low specific surface areas below 30–40 m^2/g due to the high temperature treatment required to obtain suitably crystalline samples, except for the case of the reactive grinding method. Only in recent years have mesoporous PTOs (Meso-PTOs) with exceedingly high specific surface areas reaching 100 m^2/g and well-developed mesoporosity been synthesized via solid templating synthesis using mesoporous silica as a hard template. For example, Nair et al. and Sarshar et al. synthesized mesoporous $La_{1-x}Ce_xBO_3$ (B = Co, Mn) and $LaBO_3$ (B = Mn, Co, Fe) for methane combustion and methanol oxidation [42,43]. Wang et al. synthesized mesoporous $LaCoO_3$ for methane combustion [44] and Zhao et al. also prepared mesoporous $LaFeO_3$ via a nanocasting route which showed excellent performance in humidity sensing applications [45]. Among these developments, it appears that nanocasting could be a viable method to synthesize mesoporous mixed metal perovskite-based catalysts optimized for STA reactions. Therefore, in the present work, we prepared Co–Cu- and Fe–Cu-type mesoporous perovskite materials, $LaCo_{0.7}Cu_{0.3}O_3$ and $LaFe_{0.7}Cu_{0.3}O_3$, using the nanocasting synthesis. Furthermore, we focus our investigations on the influence of the textural properties of the mesoporous perovskite catalysts (Meso-PTOs) and the process parameters on the direct conversion of syngas to alcohols, which are investigated in a fixed-bed reactor.

Experimental details

Synthesis of Meso-PTOs

A series of Meso-PTOs were synthesized using a modified templating synthesis [42]. Before starting the hard template synthesis, a KIT-6 (the three-dimensional (3-D) cubic *Ia*-3*d* structure) ordered mesoporous silica (OMS) template was synthesized according to the method in a previous report [7], except for the higher hydrothermal temperature at 130 °C. The synthesis procedure of the Meso-PTOs is briefly described here. First, a citrate complex of metal cations was used as the perovskite precursor. The precursor was impregnated into the KIT-6 template by a wet impregnation method. The chemical compositions of PTOs ($LaCo_{0.7}Cu_{0.3}O_3$ and $LaFe_{0.7}Cu_{0.3}O_3$) were selected following previous literature suggesting these compositions to be most suitable [30,33]. In a typical synthesis step for mesoporous $LaCo_{0.7}Cu_{0.3}O_3$, $La(NO_3)_3{\cdot}6H_2O$ (4.8 mmol), $Co(NO_3)_2{\cdot}6H_2O$ (3.36 mmol), and $Cu(NO_3)_2{\cdot}3H_2O$ (1.44 mmol) were dissolved in an ethanol/water mixture solution (15 ml/5 ml) of citric acid to obtain an equimolar solution, which was added slowly to KIT-6 (2 g) dispersed in water (20 ml). The molar ratio of La metal ions and citric acid was varied from 1:1 to 1:2. The mixture was stirred overnight at room temperature, after which the solvent was evaporated under a vacuum using a rotary evaporator. The powder thus obtained was further dried at 80 °C for 24 h, ground well in a mortar, and calcined at 500 °C for 4 h to remove the organic part. Impregnation was repeated twice, using for the second time one half of the amount of the precursor, to achieve higher loadings. The final powder was calcined at 700 °C for 6 h, and the silica template was then removed by treating the composite three times with NaOH (2 M) at room temperature. The obtained product was washed with water and ethanol and dried overnight at 80 °C. The resultant Meso-PTOs are denoted as Meso-CoCu-CA1 and Meso-CoCu-CA2 to represent ratios of the La metal ions to citric acid (CA) of 1:1 and 1:2, respectively. The synthesis of mesoporous $LaFe_{0.7}Cu_{0.3}O_3$ follows the same protocol described above, except that the Co precursor was replaced by the Fe precursor, $Fe(NO_3)_3{\cdot}9H_2O$. For comparison, bulk $LaCo_{0.7}Cu_{0.3}O_3$ and $LaFe_{0.7}Cu_{0.3}O_3$ samples were also prepared using the typical citric complex method [46]. These are denoted as Bulk-CoCu and Bulk-FeCu, respectively.

Characterization

Powder X-ray diffraction (XRD) patterns were recorded on a Rigaku Multiplex instrument using Cu-Kα radiation (λ = 0.15406 nm), operated at 40 kV and 40 mA (1.6 kW). Transmission electron microscopy (TEM) images were taken from the thin edges of the particles supported on a porous carbon grid using a Philips Tecnai G220 device operated at 200 kV. Scanning electron micrograph (SEM) images were obtained with a Magellan 400 scanning electron microscope operating at 10 kV. Nitrogen sorption isotherms were measured at −196 °C on a Micromeritics Tristar 3000 volumetric adsorption analyzer. Before the adsorption measurements, all samples were outgassed at 300 °C in a degassing station. The Brunauer–Emmett–Teller (BET) equation was used to calculate the apparent surface area from the adsorption data obtained at a P/P_0 ratio between 0.05 and 0.2. The total volume of micro- and mesopores was calculated from the amount of nitrogen adsorbed when $P/P_0 = 0.95$, assuming that adsorption on the external surface was negligible compared to adsorption in the pores. The pore size distributions (PSDs) were calculated by analyzing the adsorption branch of the N_2 sorption isotherm using the Barret–Joyner–Halenda (BJH) method. The actual compositions of Meso-PTO catalysts were verified by inductively coupled plasma atomic emission spectrometry (ICP-AES, Spectro Ciros Vision). The XPS (ESCALAB 250, UK) investigation was carried out using a monochromic Al Kα X-ray source (E = 1486.6 eV) and the data was processed with the XPSPEAK software. The binding energy of the C 1s peak at 284.5 eV was taken as an internal standard and the background was fitted by the Shirley method. Coke deposition of the catalyst was investigated by recording weight changes on a thermogravimetric analyzer (TA Instruments TGA Q500).

Catalytic tests

CO hydrogenation was performed in a lab-made fixed-bed reactor system [7]. To avoid reaction by the stainless steel reactor, the reactor was designed with an 8 mm inner diameter and a 35 cm copper tube inside the stainless steel tube. The end of the tube is properly welded to seal any gaps between the stainless steel tube and the copper tube. The reaction temperature was controlled by a type-K thermocouple (Omega) and PID controller. Syngas ($H_2/CO = 2$) was fed into the catalytic reactor at 60 ml/min with a mass flow controller (MFC). The catalyst (0.3 g) was loaded in the middle of the reactor and quartz wool was used to fill the length of the reactor. Before the CO hydrogenation reaction, the catalyst went through an H_2 reduction step at a 10 ml min^{-1} flow at 330 °C (heating rate: 1.5 °C/min) for 3 h. After reduction, the temperature of the reactor was cooled to room temperature for the removal of the adsorbed H_2 gas using N_2 as a sweep gas. This CO hydrogenation reaction was performed at a gas hourly space velocity (GHSV) of 12,000 h^{-1} at 320 °C under 3.0 MPa. The effluent products were kept at 200 °C by line heating and measured by an on-line gas chromatograph (6100GC, Young Lin Instruments, Co.) equipped with a thermal conductivity detector

(TCD) and a flame ionization detector (FID). The H_2, CO, CO_2, and CH_4 contents in the effluent products were detected by TCD using two capillary columns in a series in a molecular sieve 5A column (3.175 mm id × 1.83 m) and a Porapak-Q column (3.175 mm id × 1.83 m); alcohols, other oxygenates, and hydrocarbons were detected by means of FID using two packed columns in series and with a DB-FFAP (0.320 mm id × 30 m) column and HP-PLOT-Q column (0.530 mm id × 30 m). The CO conversion and production carbon selectivity levels were calculated using equations described in the literature [47],

$$\text{CO conversion } (\%) = \sum n_i \cdot C_i / (\sum n_i \cdot C_i + C_{CO}) \times 100$$

$$S_i \text{ (mol-C\%)} = n_i \cdot C / \sum n_i \cdot C_i \times 100$$

where S_i is the selectivity of carbon-containing product i, n_i is the number of carbon atoms in the product i, C_i is the molar concentration of product i, and C_{CO} is the molar concentration of unreacted CO. For the investigation of the effect of the reaction conditions, the CO hydrogenation reaction was utilized with different reaction conditions, i.e., different temperatures, pressures, and space velocities in this case. One catalyst was applied to one single test set of a reaction condition. The value of the reaction condition was changed from low to high. For example, the reaction temperature was changed from 280 °C to 340 °C. In addition, before changing to a higher temperature, we monitored the stability of CO conversion for two to three hours.

Results and discussion

Properties of Meso-PTO catalysts

Four different Meso-PTO samples were prepared via the hard-templating method using KIT-6 mesoporous silica. In this study, the KIT-6 template was hydrothermally treated in a Teflon-lined autoclave at 130 °C to obtain large mesopores. These enlarged mesopores are converted to thicker frameworks of PTOs, which could provide good structural stability during the OMS template removal step. The synthesis of Meso-PTOs consisted of repeated impregnation with the citrate complex of the desired metal cations, followed by a calcination process. As shown in the upper images in Fig. 1, the XRD patterns of the Meso-PTO samples show a single diffraction peak in the low-angle region. The peaks are weak and broad compared to the parent silica template, KIT-6. Except for the Meso-CoCu-CA2 sample, the peak position of the single XRD peak around 2 theta = 1.0° of all other samples would be indexed to the (211) reflection by the determination of the main peak position of the KIT-6 template (2 theta = ~0.9°). After template synthesis, the XRD peak usually shifts to a higher angle due to the structural contraction and strain caused by the repeated thermal treatment and the formation of the metal oxide crystal domains from the metal citrate precursors. The Meso-CoCu-CA2 sample exhibits a very weak peak at approximately 2 theta = 0.8°, which indicates relatively less well-defined mesoporosity compared to the other samples. This sample also shows the broadest pore size

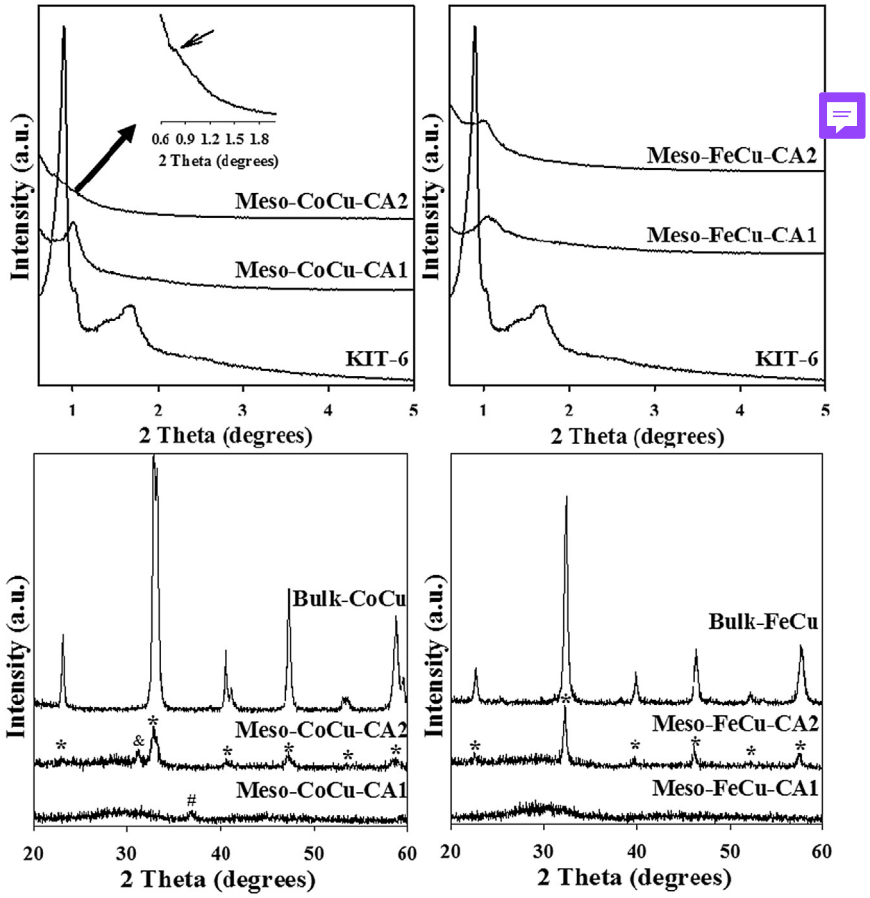

Fig. 1. Low-angle XRD patterns of KIT-6 mesoporous silica template and Meso-PTOs (top), and wide-angle XRD patterns of Bulk-PTOs and Meso-PTOs (bottom) (*: perovskite; #: CuO; &: La_2O_3).

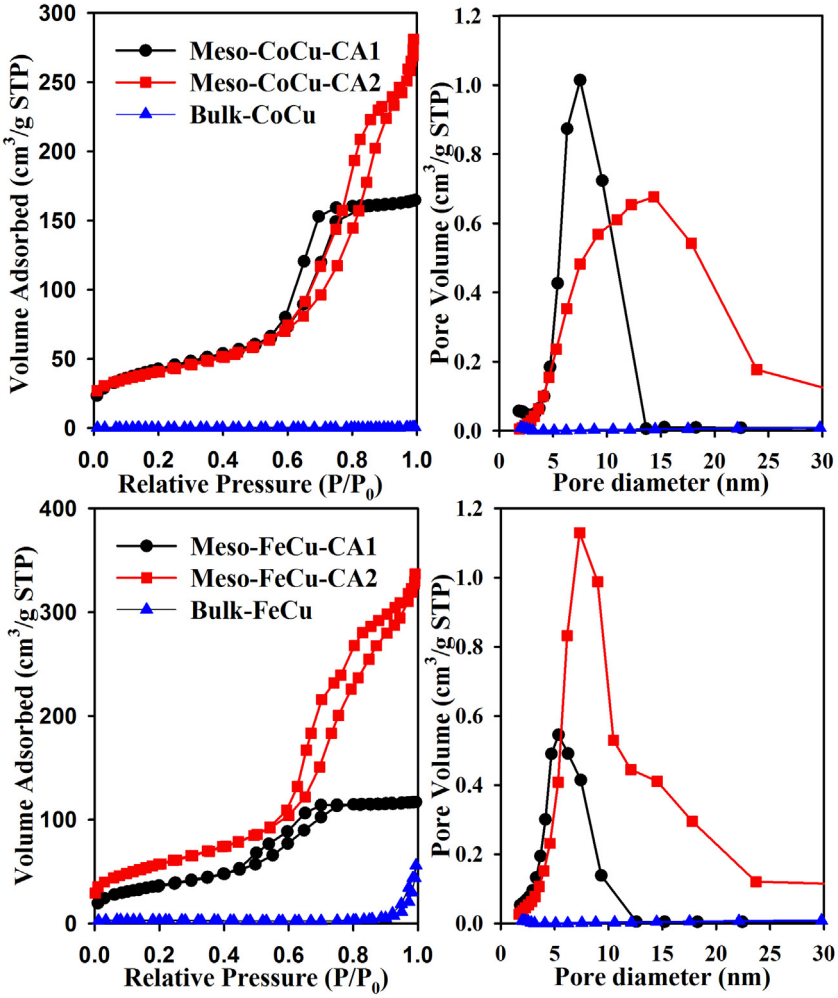

Fig. 2. N_2 sorption isotherms and respective pore size distributions of Bulk-CoCu and Meso-CoCu samples (top), and Bulk-FeCu and Meso-FeCu samples (bottom).

distribution, as shown in Fig. 2, which provides additional information regarding the less well-defined mesoporosity of the Meso-CoCu-CA2 sample.

Wide-angle XRD patterns of the Meso- and Bulk-PTO samples are shown in the lower images in Fig. 1. The XRD patterns of the Bulk-CoCu and Bulk-FeCu samples are nearly identical to those reported previously [30,33]. These patterns show the strong reflections of perovskite-type mixed oxides, with the typical orthorhombic symmetry of a perovskite-type phase. The Meso-CoCu-CA1 and Meso-FeCu-CA1 samples prepared with low amounts of citric acid (La^{3+}:CA = 1 molar ratio) show no distinct XRD peak diffraction of perovskite-type metal oxides. Only one small and broad XRD peak was noted in the Meso-CoCu-CA1 sample, which can be assigned to the presence of a small amount of copper oxides. Amorphous mixed-oxide materials, as determined by XRD diffraction, were obtained with low amounts of CA, similar to earlier perovskite synthesis results without citric acid [43]. In addition, a broad peak with very low intensity around 2 theta = 27–33° was also present, indicating the occurrence of amorphous residual silica or silicates. From the elemental analysis of these samples (Table S1 in Supplementary material), the amounts of the Si element were found to be approximately 4.1–5.2 wt% irrespective of a further extensive treatment with 2 M NaOH. This findings stem from the existence of insoluble rare-earth silicates from the strong interaction between the rare-earth elements and silica [42]. In contrast, the samples with a high amount of CA (La^{3+}:CA = 2 molar ratio) exhibit characteristic XRD peaks corresponding to the perovskite structure. The XRD peaks for Meso-CoCu-CA2 and Meso-FeCu-CA2 in the wide-angle XRD region are smaller and weaker than those of the bulk perovskite samples, indicating the formation of relatively small perovskite crystal domains in the Meso-PTOs.

As shown in Fig. 2, all of the prepared samples exhibit a type IV isotherm shape with a hysteresis loop, indicative of the existence of mesopores. The size of the hysteresis loop for the Meso-PTO-CA2 samples is larger than that for the Meso-PTO-CA1 samples, which reflects a broader pore size distribution. The pore size distribution profiles (Fig. 2, right) clearly show that the samples with a low amount of CA have a narrower pore size distribution compared with the samples obtained with high CA amounts. This well-defined mesoporosity for Meso-PTO-CA1 may have originated from the fact that the frameworks are composed of amorphous-like mixed-metal oxides, whereas the Meso-PTO-CA2 samples have small crystal domains of perovskite-type mixed oxides. With an increase in the material crystallinity, the degree of mesoporosity of the final template-free material usually decreased during the template synthesis step. This may have been caused by structural strain from the formation of a crystal domain that may have led to the collapse of the ordered mesoporosity. Among the two Meso-PTO-CA2 samples, Meso-FeCu-CA2 sample has a more uniform pore size distribution than the Meso-CoCu-CA2 sample. The detailed physicochemical properties of the Bulk-PTO and

Table 1
Physicochemical properties of Bulk-PTOs and Meso-PTOs.

Samples	S_{BET} ($m^2 g^{-1}$)[a]	V_t ($cm^3 g^{-1}$)[a]	w_{BJH} (nm)[a]	w_{avg} (nm)[a]
Bulk-CoCu	9.1	0.02	–	–
Meso-CoCu-CA1	155	0.25	7.5	6.0
Meso-CoCu-CA2	146	0.37	14.3	10.4
Bulk-FeCu	10.0	0.02	–	–
Meso-FeCu-CA1	132	0.18	5.4	4.7
Meso-FeCu-CA2	207	0.46	7.3	8.2
GM[b]	21.5	–	–	18.0[c]

[a] S_{BET}, apparent BET specific surface area; V_t, total pore volume; w_{BJH}, pore size calculated using the BJH method and deduced from the highest point of pore size distribution curve; w_{avg}, average pore size.
[b] GM, the $LaCo_{0.7}Cu_{0.3}O_3$ sample synthesized by the reactive grinding in Ref. [33].
[c] Pore diameter determined form N_2 adsorption/desorption isotherms in Ref. [33].

Meso-PTO samples from the N_2 sorption analyses are listed in Table 1. The specific BET surface areas and pore volumes of the Meso-PTO samples are in the ranges of 132–207 m^2/g and 0.18–0.46 cm^3/g, respectively These values are significantly higher than those of Bulk-PTO materials and GM, which was synthesized by reactive grinding [33].

Fig. 3 shows the TPR-H_2 profiles of the prepared Bulk-PTOs and Meso-PTOs. Bulk-CoCu prepared by the citric acid method shows one broad main peak with a maximum around 240 °C, which is ascribed to the two successive reductions of Cu^{2+} and Co^{3+} in the perovskite lattice [33,48]. Metallic copper and cobalt are formed in the reduction temperature ranges of approximately 350–450 °C and greater than 500 °C [48,49]. The Meso-CoCu-CA2 sample has a TPR profile similar to that of the Bulk-CoCu sample. However, the Meso-CoCu-CA1 samples show two distinct and separate peaks for the reductions of Cu^{2+} (193 °C) and Co^{3+} (280 °C) [32]. In addition, the small shoulder peak of the Meso-PTO samples at 146 °C can be attributed to the reduction of an extra-framework or separated copper oxide. The shift of the reduction peaks for Cu^{2+} and Co^{3+} in the Bulk-CoCu and Meso-CoCu-CA2 samples, in comparison to the Meso-CoCu-CA1 sample, is attributed to the close vicinity and electronic interaction of two metal ions in the perovskite lattice, and promoting the reducibility of the cobalt ions by the reduced copper species [32]. From these TPR results, the Meso-CoCu-CA2 and Meso-CoCu-CA1 samples consist of a perovskite-type structure and a mixed oxide phase, respectively, which is in agreement with the powder wide-angle XRD results shown in Fig. 1. For the La–Fe–Cu oxide samples, one obvious reduction peak can be observed in the TPR profiles, which is the well-known reduction peak for Cu^{2+} in the perovskite structure. Bulk-FeCu shows a main sharp peak with a shoulder at a maximum of 275 °C for the overlapping reduction of the lattice Fe^{4+} and Cu^{2+} [30,48]. The broad peak around 340–600 °C corresponds to the reduction of Fe^{3+} cations in the perovskite lattice to Fe^{2+} and the formation of metallic Cu^0 from Cu^+ [48,50]. The Meso-FeCu-CA1 sample with a low CA amount (La^{3+}:CA = 1) also shows one sharp peak at 265 °C and one broad peak with weak intensity around 340–460 °C (centered at 380 °C). Meso-FeCu-CA2 prepared with a greater amount of citric acid shows distinct reduction peaks at around 140 °C and 275 °C for the reduction of extra-framework Cu^{2+} and intra-framework Cu^{2+}/Fe^{4+}, respectively. The temperature range of the reduction peak for Fe^{3+} is around 340–440 °C (a weak peak centered at 370 °C). With an increase in the amount of citric acid used during the synthesis of the Meso-FeCu samples, the reduction peaks of the Cu^{2+} and Fe^{3+} cations in the Meso-FeCu-CA2 sample shift to higher and lower temperatures, respectively, as compared with the Meso-FeCu-CA1. This may be due to electronic interactions between Cu^{2+} and Fe^{3+} species in the perovskite lattice, making the iron ions more easily reducible by the reduced copper [51].

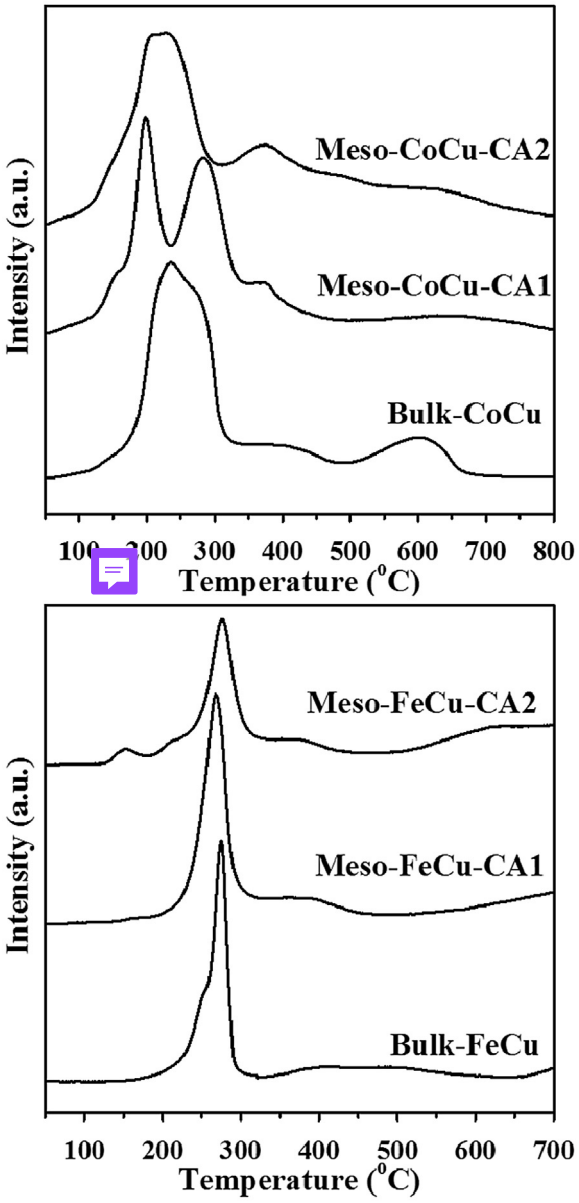

Fig. 3. TPR results of Bulk-CuCo and Meso-CuCo samples (top), and Bulk-FeCo and Meso-FeCo samples (bottom).

TEM analyses were conducted to visualize the mesoscopic order of the prepared Meso-PTO samples. The resulting TEM images are shown in Fig. 4. Regular mesostructural pore ordering is clearly observed in some of the domains of the samples, but disordered or less defined mesoporous regions are also present, except for the Meso-CoCu-CA2 sample. In this latter case, most regions have a disordered mesoporous structure. This may be related to the very weak peak in the low-angle XRD pattern (Fig. 1) of this material compared to that of the other samples. Representative SEM images of the Bulk-FeCu, and the Meso-FeCu-CA2 sample are shown in Fig. 5. The SEM image of the Bulk-FeCu sample showed amorphous slit- or plate-like morphologies, similar to the Bulk-CoCu sample as shown in Fig. S1 in Supplementary material. On the other hand, the Meso-FeCu-CA2 sample exhibited SEM images similar to those of the KIT-6 template (Fig. S1 in Supplementary material), and the other Meso-PTO samples also had a comparable morphology to the KIT-6 silica template. Such similarities of the morphologies

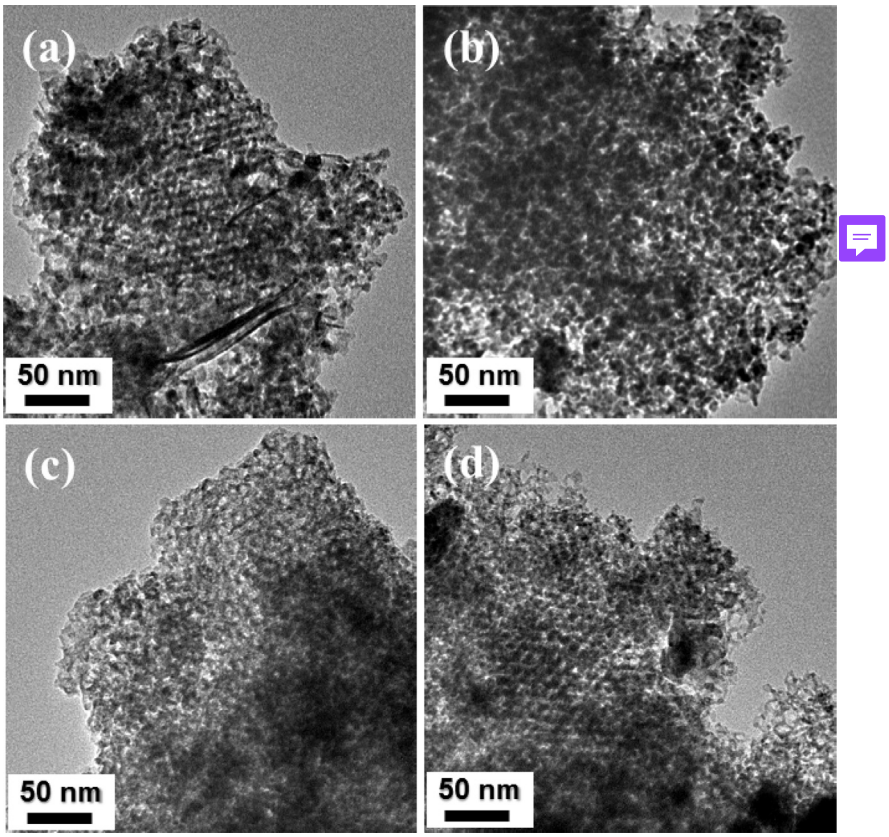

Fig. 4. TEM images of (a) Meso-CoCu-CA1, (b) Meso-CoCu-CA2, (c) Meso-FeCu-CA1, and (d) Meso-FeCu-CA2.

between the silica template and the resultant mesoporous perovskite-type oxide samples are in line with the successful network replication process occurring during the hard-templating synthetic route, which also ensures efficient particle morphology replication [52–54].

Effects of Meso-PTOs on STA activity

Fig. 6 and Table 2 show the CO conversion, higher alcohol selectivity and productivity of the Bulk-PTO and Meso-PTO catalysts during the CO hydrogenation reaction. The detailed catalytic performances and product selectivities of these catalysts are compiled in Table S2 in Supplementary material. Among the catalysts with the La–Co–Cu composition, the observed CO conversion and $C_{2-4}OH$ space-time-yield (STY) of Meso-CoCu-CA1 were higher than those of the Bulk-CoCu and Meso-CoCu-CA2 samples, even if this catalyst did not have a perovskite-type structure. This outcome indicates that the presence of a perovskite structure is not necessary to increase the STA catalytic performance in the La–Co–Cu catalytic system. Between the two perovskite-type catalysts (Bulk-CoCu and Meso-CoCu-CA2) the STY for higher alcohols of Meso-CoCu-CA2 is greater than that of Bulk-CoCu despite the fact that the $C_{2-4}OH$ selectivity appears lower, which can be attributed to the higher CO conversion of the Meso-CoCu-CA2 PTO catalyst (~1.4 times higher) compared to the Bulk-CoCu PTO catalyst. The high CO conversion of the Meso-CoCu-CA2 catalyst could mainly be due to the larger specific surface area from the mesoporous PTO structure in the Meso-CoCu-CA2 sample compared to that of the Bulk-CoCu sample. Interestingly, the non-PTO structure, Meso-CoCu-CA1 (mixed-metal oxides with an amorphous phase as determined by XRD analysis), has the highest CO conversion and a high STY of higher alcohols with $C_{2-4}OH$

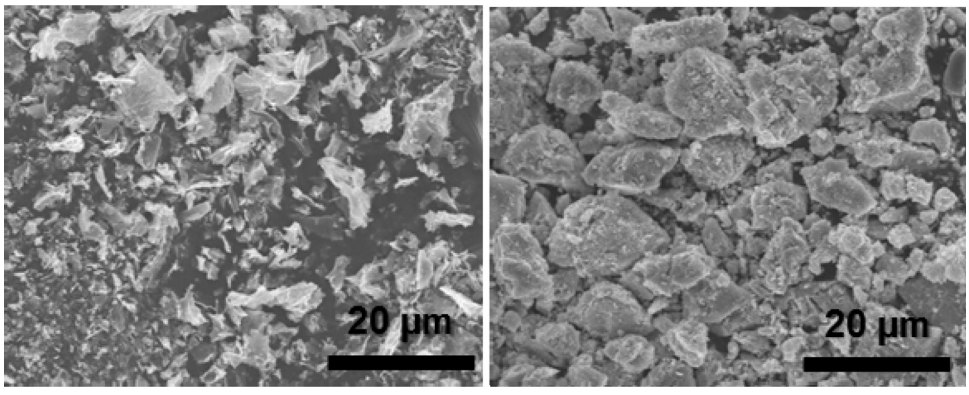

Fig. 5. SEM images of Bulk-FeCu (left) and Meso-FeCu-CA2 (right).

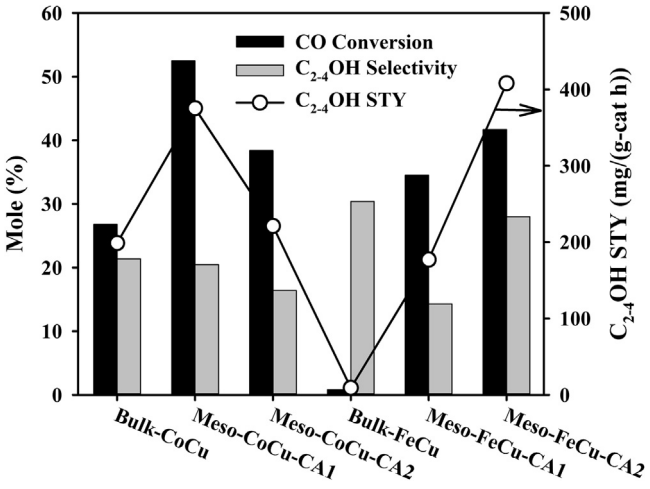

Fig. 6. CO conversion and selectivity and space-time-yield (STY) of C_{2-4} alcohols for Bulk- and Meso-PTO catalysts.

selectivity similar to that of the Bulk-CoCu catalyst in the La–Co–Cu composition. This phenomenon implies the formation of highly dispersed monometallic (Co, Cu) or bimetallic (Co–Cu) oxide species as a catalytically active component of STA during the reaction. This could be correlated with perovskite- (La_2O_3, $LaCoO_3$), and silica- and carbon- (CNT) supported Co or Cu catalysts as reported in the literature for the synthesis of higher alcohols from syngas [24,31,35,55,56]. However, in our case, further investigations would be required to clarify this catalytic behavior and to verify the hypothesis of CoCu nanoparticle formation in the case of the Meso-CoCu-CA1 catalyst.

For the other catalytic composition, La–Fe–Cu, the two mesoporous materials (Meso-FeCu-CA1 and Meso-FeCu-CA2) show superior CO conversion rates in the STA reaction compared to those of the Bulk-FeCu catalysts owing to their high surface areas and well-developed mesoporosity. The order of the CO conversion of these catalysts is Meso-FeCu-CA2 > Meso-CoCu-CA1 >> Bulk-FeCu. The Bulk-FeCu catalyst shows almost no catalytic activity below 1% of CO conversion but still exhibits good product selectivity for higher alcohols. Interestingly, the perovskite structure composed of La, Fe, and Cu reveals the lowest selectivities of methane and C_{2+} hydrocarbons in addition to the highest selectivity of total alcohols (C_{1-4} alcohols). This product selectivity distribution clearly indicates that the perovskite $LaFe_{0.7}Cu_{0.3}O_3$ material suppresses the formation of methane via the methanation reaction and facilitates CO insertion into the surface absorbed alkyl species ($^*C_xH_y$) for the formation of alcohols. The non-perovskite-type sample (Meso-FeCu-CA1) shows a much higher CO conversion, but it has less than half of the selectivity toward C_{2-4}OH compared with the Bulk-FeCu catalyst. Almost half of the syngas is converted over the Meso-FeCu-CA1 catalyst into methane via the methanation reaction (selectivity of CH_4 = 46.7%), which is considered as the worst side-reaction during the STA reaction because the feed gas (syngas, mixture of CO and H_2) is typically prepared by methane reforming. After CO dissociation on the surface of the catalyst in the STA reaction, the adsorbed surface carbide species (C^*) is successively hydrogenated by the adsorbed surface hydrogen atom (H^*), after which methane is finally formed. This process is similar to the reverse reaction of methane decomposition using a FeCu-type catalyst [57]. The Meso-FeCu-CA2 sample clearly shows the greatest increase of CO conversion (a 40.9% increase) with a slight decrease in the C_{2-4}OH selectivity (a 2.4% decrease) compared to the Bulk-FeCu sample. This can be attributed to the characteristic structure of Meso-FeCu-CA2, which

Table 2
Catalytic activities of Bulk and Meso-PTO catalysts at 18 h.

Catalyst	CO Conv. (%)	C_{2-4}OH STY[a] (mg/(g-cat h))	Carbon selectivity (mol C%)			
			CH_4	MeOH	C_{2-4}OH[b]	Other C_{2+}oxy[c]
Bulk-CoCu	26.8	198.8	34.7	0.3	21.4	17.4
Meso-CoCu-CA1	52.5	375.3	34.3	0.3	20.5	17.7
Meso-CoCu-CA2	38.4	221.0	39.0	2.7	16.4	17.2
Bulk-FeCu	0.8	8.9	14.8	26.9	30.4	8.0
Meso-FeCu-CA1	34.5	177.2	46.7	1.8	14.3	11.4
Meso-FeCu-CA2	41.7	408.1	19.7	2.4	28.0	17.9

[a] C_{2-4}STY, space-time-yield of C_{2-4} alcohols.
[b] C_{2-4}OH, alcohols with 2–3 carbons.
[c] Other C_{2+}oxy, oxygenates with more than two carbon atoms.

has both mesoporosity and a perovskite-type phase. Mesoporosity with a high surface area and relatively uniform mesopores could increase the overall catalytic activity of the Meso-FeCu-CA2 material (e.g., CO conversion) owing to the presence of considerable numbers of active sites and facile mass transport compared to the Bulk-FeCu catalyst. The perovskite structure of Meso-FeCu-CA2 could preserve the good C_{2-4}OH selectivity of the Bulk-FeCu catalyst. Thus, these synergetic effects of the mesoporosity and the perovskite structure finally provide the highest C_{2-4}OH productivity (C_{2-4}OH STY = 408.1 mg/(g_{-cat} h)) among all of the catalysts prepared in this work. In addition, the methanation reaction was still suppressed over the Meso-FeCu-CA2 catalyst, and the methane selectivity remained below 20%. From the detailed product selectivities shown in Table S2 in Supplementary material, the Meso-FeCu-CA2 sample also demonstrates lower methanol selectivity and higher C_4OH and C_{4+}oxy selectivity levels compared to the Bulk-FeCu catalyst. It is plausible that additional reactions of carbon chain growth were facilitated over Meso-FeCu-CA2 before CO insertion in comparison to the outcome with the Bulk-FeCu catalyst. When comparing the catalytic results between the two mesoporous PTO samples (Meso-CoCu-CA2 and Meso-FeCu-CA2) in Tables 2 and S2, the effect of the different metal (Co and Fe) cations dispersed in the perovskite lattice on the STA reaction could originate from the fact that Co species in the PTO lattice facilitated the methanation reaction, whereas the Fe species appeared to suppress the methanation reaction and enhance carbon growth and CO insertion reactions after the C-O dissociation of the carbon monoxide.

The surface basicity of the samples was analyzed by CO_2-TPD (Fig. S2 in Supplementary material) because the carbon chain growth for higher alcohol synthesis could also occur via base-catalyzed aldol condensation [58–60]. One CO_2 desorption peak was observed around 100 °C for the Meso-CoCu-CA2 and Meso-FeCu-CA2 samples. This represents weak basic sites on the surface of these samples. Meso-CoCu-CA2 and Meso-FeCu-CA2 samples showed two desorption peaks at around 100 °C and 180 °C. The additional CO_2 desorption peak at 180 °C indicates that the existence of relatively stronger basic sites in the Meso-PTO-CA2 samples compared with the Meso-PTO-CA1 samples. This result revealed a contribution of somewhat stronger basic sites related with the crystallinity of the Meso-PTO samples. Low crystalline nature of the mixed oxide Meso-PTO-CA1 samples could permit adsorbing additional CO_2. Considering of the catalytic results in Table 2 with these surface basicity properties, the weak basic property of all the Meso-PTO catalysts may not have an effect on the selectivity towards higher alcohols via base-catalyzed aldol condensation.

Fig. 7 shows the CO conversion and the STY for C_{2+} alcohol with the time-on-stream (TOS) of the STA reaction over the Meso-PTO

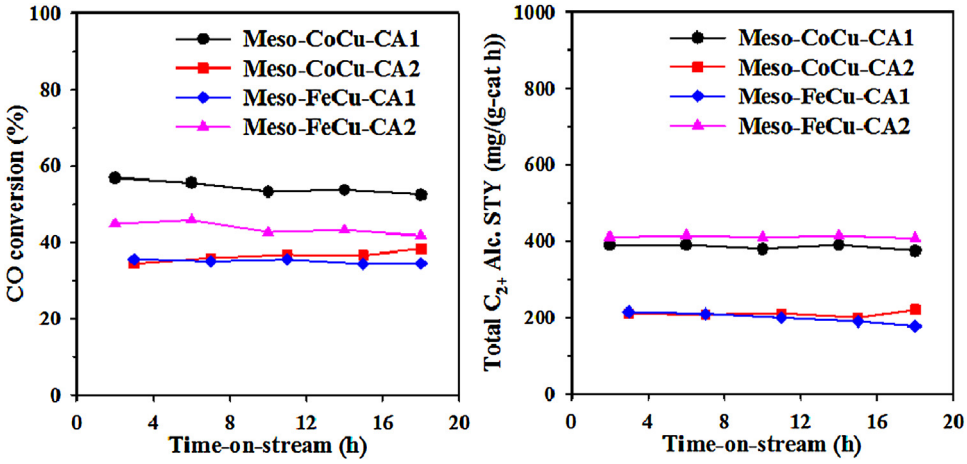

Fig. 7. CO conversion and total C_{2+} alcohol STY over Meso-PTO catalysts with time-on-stream at 320 °C, 3.0 MPa, GHSV of 12,000 h^{-1}.

catalysts. The catalysts exhibited constant CO conversion and C_{2+} alcohol STY throughout the reaction period. These results imply that all of the catalysts with a mesoporous structure are stable and preserve their catalytic activity without distinct deactivation throughout the reaction. Fig. S3 in Supplementary material is a representative TEM image of the spent Meso-FeCu-CA2 catalyst after the STA reaction. The TEM image clearly shows that the mesoporous structure of the Meso-FeCu-CA2 catalyst does not collapse or deform into a non-mesoporous structure under the reaction conditions of the STA process, providing a good clue about the stability of these catalysts. As shown in Fig. S4 in Supplementary material, the wide-angle XRD pattern of the spent Meso-FeCu-CA2 catalyst was nearly identical to that of the fresh catalyst. Therefore, one can conclude that the perovskite structure of the Meso-FeCu-CA2 catalyst was preserved during the course of the STA reaction. Moreover, the amount of coke which formed for the spent Meso-FeCu-CA2 catalyst after the 18 h reaction was estimated by a TGA analysis, as illustrated in Fig. S5 in Supplementary material. The weight loss in the temperature range of 260–600 °C was 1.0 wt%. From these TGA results, only a small amount of coke was formed, serving as an indication of good catalytic longevity as well as good catalytic activity of the Meso-FeCu-CA2 catalyst during the STA reaction.

Fig. S6 in Supplementary material shows the XPS spectra of the fresh and spent Bulk-CoCu, Bulk-FeCu, Meso-CoCu-CA1, and Meso-FeCu-CA2 catalysts. A detailed discussion of these XPS spectra is given in Section S2 in the Supplementary Materials section. In the cobalt 2p XPS spectra of the fresh Bulk-CoCu and Meso-CoCu-CA1 materials, both Co^{2+} and Co^{3+} species are present in the fresh La–Co–Cu oxide-type catalysts. The spent Bulk-CoCu and Meso-CoCu-CA1 catalysts only exhibited Co^{2+} species, indicating that the La–Co–Cu oxide-type catalysts maintained the Co^{2+} species during the STA reaction. The Co^{3+} species may have been converted during the hydrogen pretreatment at 330 °C, thus retaining their state during the STA reaction. For the Cu 2p spectra in the Bulk-CoCu and Meso-CoCu-CA1 catalysts, Cu^{2+} species existed in both the fresh Bulk-CoCu and the Meso-CoCu-CA1 samples. However, Cu^0 species were found in the spent Meso-CoCu-CA1 catalyst. The observed Cu^0 species in the spent Meso-CoCu-CA1 catalyst could explain the lowest reduction temperature of the extra-framework or separate copper oxide in the TPR profile of the fresh Meso-CoCu-CA1, as shown in Fig. 3. These XPS and TPR results for Meso-CoCu-CA1 suggest that the formation of Cu^0 species most likely occurred after the hydrogen pretreatment, with the low-valence Cu^0 state preserved during the STA reaction. This may thus be related to the high catalytic activity of this Meso-CoCu-CA1 sample with a non-PTO structure compared to the Bulk- and Meso-PTO catalysts, as discussed above in Section "Effects of Meso-PTOs on STA activity". The wide-angle XRD pattern of the spent Meso-CoCu-CA1 in Fig. S4 in Supplementary material shows a XRD pattern similar to that observed for the fresh Meso-CoCu-CA1, which reveals an amorphous phase of metal oxides. However, the small and broad peak for CuO in the fresh Meso-CoCu-CA1 disappeared after the STA reaction. From the Cu 2p XPS spectra, these CuO species may be converted to metallic Cu; however, no distinct metallic Cu peaks were observed in the XRD pattern of the spent sample. This would suggest the presence of highly dispersed Cu metal in this catalyst without aggregation during the STA reaction. For the spent Bulk-CoCu catalyst, the XPS spectra show the existence of Cu^{2+} and Cu^+ species. For the fresh and spent Bulk-FeCu and Meso-FeCu-CA2 catalysts, the Cu 2p spectra also show features similar to those of the fresh and spent Bulk-CoCu catalysts. These findings indicate that the spent Bulk-CoCu, Bulk-FeCu, and Meso-FeCu catalysts may all retain both the Cu^+ and the Cu^{2+} species during the STA reaction, but the amount of the Cu^+ species appeared to be greater than that of Cu^{2+} according the greater XPS peak area of Cu^+ compared to that of Cu^{2+}. The Fe 2p peaks of the fresh Bulk-FeCu and Meso-FeCu-CA2 catalysts showed Fe^{2+} and Fe^{3+} components [61]. After the STA reaction, the spent catalysts also showed similar Fe 2p peaks, as observed in the fresh catalyst. This is a strong indication that the Fe chemical states did not change during the reaction.

Effects of the Meso-FeCu-CA2 with different reaction conditions

In order to investigate the reaction conditions for high productivity of higher alcohols, the best catalyst, Meso-FeCu-CA2, was applied in the CO hydrogenation reaction under different reaction conditions, that is, different reaction temperatures, pressures, and space velocities of the gas feed. As shown in Fig. 8, the catalyst was tested at various temperatures ranging from 280 to 340 °C (other reaction conditions: 3 MPa and a GHSV of 12000 h^{-1}). The conversions of CO of both catalysts increased with an increase in the temperature due to the high activation energy for the dissociation of adsorbed CO on the surfaces of the catalysts. These CO conversions show sharp increases from 310 °C to 320 °C. Moreover, the productivity of higher alcohols (C_{2-4}OH STY) for the Meso-FeCu-CA2 catalyst shows a similar trend to the CO conversion, as the selectivities to the products are not greatly changed with different temperatures. In the detailed product selectivities reported in Table S3 in Supplementary material, CO_2

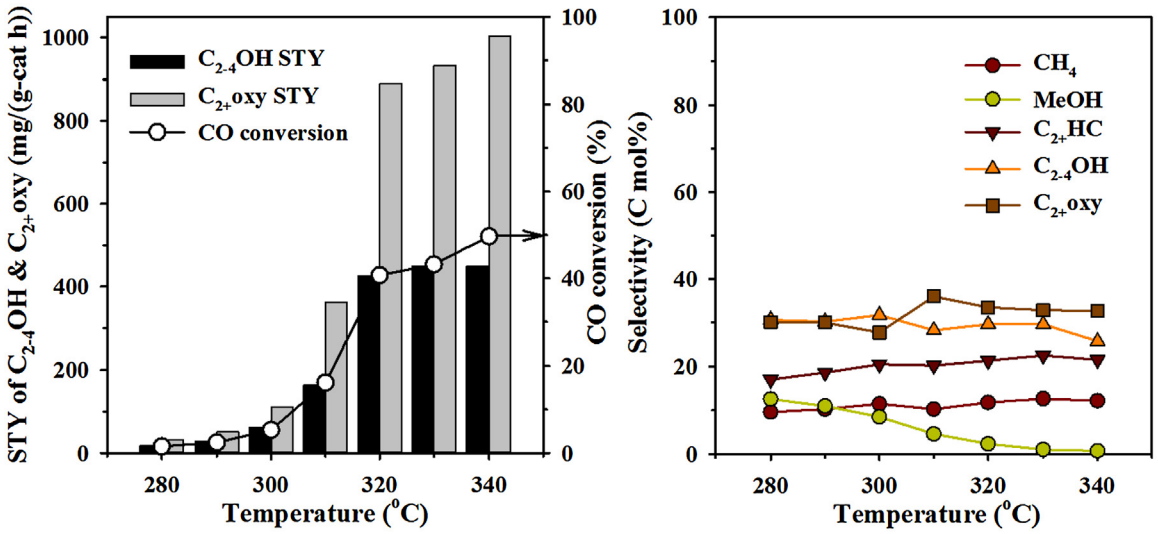

Fig. 8. CO conversion, C_{2-4}OH STY, C_{2+}oxy STY, and selectivity to CH_4, MeOH, C_{2+}HC, C_{2-4}OH, and C_{2+}oxy with reaction temperature (280–340 °C) over Meso-FeCu-CA2 at 3.0 MPa, GHSV of 12000 h^{-1}.

does not appear in this range of low reaction temperatures below 310 °C. The selectivity to carbon dioxide only increases with an increase in the temperature in the range of 310–340 °C. We attribute this behavior to water which may have formed during the STA reaction, and applying a higher temperature may facilitate the conversion of this water (together with CO) into CO_2 via a water-gas-shift reaction [32].

Fig. S7 in Supplementary material shows the catalytic activity of the Meso-FeCu-CA2 catalyst under various pressures ranging from 2 to 5 MPa (320 °C, and GHSV of 12000 h^{-1}). An increase in the reactor pressure from 2 to 5 MPa gradually increases both the conversion of CO and the productivities of the higher alcohols and C_{2+} oxygenates. A similar trend to the effect of reaction temperature was also observed. The higher reactor pressure enables a more dissociative adsorption of CO on the Meso-FeCu-CA2 catalyst. Moreover, the product selectivities do not show great differences between the reactions performed at different pressures. In comparison to the temperature effect on the productivity of higher alcohols, the changes in the productivity with different pressures in the reactor are minor. This suggests that higher alcohol productivity is much more dependent on the temperature than on the pressure. Fig. S8 in Supplementary material illustrates the catalytic performance of the catalyst at different gas space velocities (GHVS) from 4000 to 12000 h^{-1} (320 °C and 3 MPa). With an increase in the syngas feed flow rate, the CO conversion and productivity of C_{2-4}OH STY and C_{2+}oxy STY both gradually decrease. This can be explained by the fact that the increased GHVS results in a decrease of the contact time between the feed gas and the catalytic active sites, possibly leading to a gradual decline in the conversion of CO. In addition, the product selectivities did not differ greatly at different feed flow rates. Thus, the productivity of higher alcohols over the Meso-FeCu-CA2 catalyst mainly depends on the CO conversion among the reaction conditions studied in this work. For a comparison of the mesoporous PTO catalyst with findings in the literature, Table S6 in Supplementary material shows the catalytic activities of typical perovskite-type oxide catalysts for the STA reaction. The Meso-FeCu-CA2 catalyst exhibits both better catalytic activity and better selectivity to higher alcohols than typical PTO catalysts.

Conclusion

For synthesis of higher alcohols, two types of mesoporous perovskite-type catalysts were prepared via a hard templating route using the citrate complexing method and a hydrothermally treated KIT-6 OMS template. These prepared catalysts have higher surface areas and larger pore volumes than bulk-PTOs due to the presence of mesopores in the materials, but the perovskite phase was only obtained during the synthesis process using a considerable amount of citric acid. These catalysts showed high catalytic performance for the production of higher alcohols and C_{2+} oxygenates compared with bulk perovskite catalysts. In particular, the mesoporous $LaFe_{0.7}Cu_{0.3}O_3$ catalyst (Meso-FeCu-CA2) showed significant suppression of the methanation reaction and an enhancement of the selective production of C_3 and C_4 alcohols as well as C_{2+} oxygenates. This result could be attributed to the high dispersion of active sites owing to high surface provided by mesoporosity in the retained perovskite structure. In addition, the production of higher alcohols is strongly dependent on the process variables when using the Meso-FeCu-CA2 catalyst. The CO conversion varies with the reaction conditions, whereas the production selectivities do not change substantially. The reaction temperature is one of the key parameters having the greatest effect on the CO conversion.

Acknowledgments

The authors would like to acknowledge the financial support from the R&D Convergence Program of the MSIP (Ministry of Science, ICT and Future Planning) and NST (National Research Council of Science & Technology) of the Republic of Korea (CRC-14-1-KRICT), and C1 Gas Refinery Program through the National Research Foundation of Korea (NRF) funded by the (2016M3D3A1A01913251). F. K. thanks the University of Vienna for the support.

Appendix A. Supplementary data

Supplementary data associated with this article can be found, in the online version, at http://dx.doi.org/10.1016/j.jiec.2017.02.032.

References

[1] V.R. Surisetty, A.K. Dalai, J. Kozinski, Appl. Catal. A 404 (2011) 1.
[2] M. Gupta, M.L. Smith, J.J. Spivey, ACS Catal. 1 (2011) 641.
[3] K. Fang, D. Li, M. Lin, M. Xiang, W. Wei, Y. Sun, Catal. Today 147 (2009) 133.
[4] V.R. Surisetty, A.K. Dalai, J. Kozinski, Energy Fuels 25 (2011) 580.
[5] G. Prieto, P. Concepción, A. Martínez, E. Mendoza, J. Catal. 280 (2011) 274.
[6] M.-J. Kim, H.-J. Chae, K.-S. Ha, K.-E. Jeong, C.-U. Kim, S.-Y. Jeong, T.-W. Kim, J. Porous Mater. (2014) 1.
[7] M.-J. Kim, H.-J. Chae, K.S. Ha, K.-E. Jeong, C.-U. Kim, S.-Y. Jeong, T.-W. Kim, J. Nanosci. Nanotechnol. 13 (2013) 7511.
[8] V. Abdelsayed, D. Shekhawat, J.A. Poston Jr., J.J. Spivey, Catal. Today 207 (2013) 65.
[9] K. Albrecht, V.-A. Glezakou, R. Rousseau, M. Engelhard, T. Varga, R. Colby, J. Jaffe, X. Li, D. Mei, C. Windisch, S. Kathmann, T. Lemmon, M. Gray, T. Hart, B. Thompson, M. Gerber, Rh-Based Mixed Alcohol Synthesis Catalysts: Characterization and Computational Report, Pacific Northwest National Laboratory, 2013.
[10] M. Gerber, M. Gray, J. White, D. Stevens, Evaluation of Promoters for Rhodium-Based Catalysts for Mixed Alcohol Synthesis, Pacific Northwest National Laboratory, 2008.
[11] M. Gerber, J. White, M. Gray, B. Thompson, D. Stevens, Optimization of Rhodium-Based Catalysts for Mixed Alcohol Synthesis – 2009 Progress Report, Pacific Northwest National Laboratory, 2010.
[12] A.L. Villanueva Perales, C. Reyes Valle, P. Ollero, A. Gómez-Barea, Energy 36 (2011) 4097.
[13] V.R. Surisetty, Y. Hu, A.K. Dalai, J. Kozinski, Appl. Catal. A 392 (2011) 166.
[14] V. Subramani, S.K. Gangwal, Energy Fuels 22 (2008) 814.
[15] J. He, W.-N. Zhang, J. Zhejiang, Univ. Sci. A 9 (2008) 714.
[16] A. Cosultchi, M. Pérez-Luna, J. Morales-Serna, M. Salmón, Catal. Lett. 142 (2012) 368.
[17] T. Ishida, T. Yanagihara, X. Liu, H. Ohashi, A. Hamasaki, T. Honma, H. Oji, T. Yokoyama, M. Tokunaga, Appl. Catal. A 458 (2013) 145.
[18] W. Gao, Y. Zhao, J. Liu, Q. Huang, S. He, C. Li, J. Zhao, M. Wei, Catal. Sci. Technol. 3 (2013) 1324.
[19] X. Yang, X. Zhu, R. Hou, L. Zhou, Y. Su, Fuel Process. Technol. 92 (2011) 1876.
[20] W. Feng, Q. Wang, B. Jiang, P. Ji, Ind. Eng. Chem. Res. 50 (2011) 11067.
[21] Q. Wu, J.M. Christensen, G.L. Chiarello, B. Temel, J.-D. Grunwaldt, A.D. Jensen, Prepr. Symp. – Am. Chem. Soc., Div. Fuel Chem. 56 (2011) 153.
[22] A. Andersen, S.M. Kathmann, M.A. Lilga, K.O. Albrecht, R.T. Hallen, D. Mei, Prepr. Symp. – Am. Chem. Soc., Div. Fuel Chem. 56 (2011) 379.
[23] X. Xiaoding, E.B.M. Doesburg, J.J.F. Scholten, Catal. Today 2 (1987) 125.
[24] K. Xiao, X. Qi, Z. Bao, X. Wang, L. Zhong, K. Fang, M. Lin, Y. Sun, Catal. Sci. Technol. 3 (2013) 1591.
[25] H. Zhang, W. Chu, H. Xu, J. Zhou, Fuel 89 (2010) 3127.
[26] M.A. Peña, J.L.G. Fierro, Chem. Rev. (Washington, DC, U. S.) 101 (2001) 1981.
[27] N. Escalona, S. Fuentealba, G. Pecchi, Appl. Catal. A 381 (2010) 253.
[28] L. Bedel, A.C. Roger, C. Estournes, A. Kiennemann, Catal. Today 85 (2003) 207.
[29] J.R. Souza, M.A.F. Melo, D.M.A. Melo, L.O.A. Rojas, C.F. Silva, F.S. Oliveira, Braz. J. Petrol. Gas 5 (2011) 1.
[30] Y.Z. Fang, Y. Liu, L.H. Zhang, Appl. Catal. A 397 (2011) 183.
[31] N.T.T.N.T. Thuan, S. Kaliaguine, VNU J. Sci. 25 (2009) 112.
[32] N. Tien-Thao, H. Alamdari, S. Kaliaguine, J. Solid State Chem. 181 (2008) 2006.
[33] N. Tien-Thao, M.H. Zahedi-Niaki, H. Alamdari, S. Kaliaguine, Appl. Catal. A 326 (2007) 152.
[34] N. Tien-Thao, M. Hassan Zahedi-Niaki, H. Alamdari, S. Kaliaguine, J. Catal. 245 (2007) 348.
[35] N. Tien-Thao, H. Alamdari, M.H. Zahedi-Niaki, S. Kaliaguine, Appl. Catal. A 311 (2006) 204.
[36] J.A. Brown Bourzutschky, N. Homs, A.T. Bell, J. Catal. 124 (1990) 52.
[37] P.R. Watson, G.A. Somorjai, J. Catal. 74 (1982) 282.
[38] V. Palomares, A. Goñi, I.G.d. Muro, I. de Meatza, M. Bengoechea, O. Miguel, T. Rojo, J. Power Sources 171 (2007) 879.
[39] R.E. Schaak, T.E. Mallouk, Chem. Mater. 14 (2002) 1455.
[40] M. Mori, N.M. Sammes, G.A. Tompsett, J. Power Sources 86 (2000) 395.
[41] R. Leanza, I. Rossetti, L. Fabbrini, C. Oliva, L. Forni, Appl. Catal. B: Environ. 28 (2000) 55.
[42] M.M. Nair, F. Kleitz, S. Kaliaguine, ChemCatChem 4 (2012) 387.
[43] Z. Sarshar, F. Kleitz, S. Kaliaguine, Energy Environ. Sci. 4 (2011) 4258.
[44] Y. Wang, J. Ren, Y. Wang, F. Zhang, X. Liu, Y. Guo, G. Lu, J. Phys. Chem. C 112 (2008) 15293.
[45] J. Zhao, Y. Liu, X. Li, G. Lu, L. You, X. Liang, F. Liu, T. Zhang, Y. Du, Sensors Actuators B: Chem. 181 (2013) 802.
[46] M.S.G. Baythoun, F.R. Sale, J. Mater. Sci. 17 (1982) 2757.
[47] S.-H. Chai, J.Y. Howe, X. Wang, M. Kidder, V. Schwartz, M.L. Golden, S.H. Overbury, S. Dai, D.-E. Jiang, Carbon 50 (2012) 1574.
[48] R. Zhang, H. Alamdari, S. Kaliaguine, J. Catal. 242 (2006) 241.
[49] N. Tien Thao, L.T. Son, J. Sci.: Adv. Mater. Devices 1 (2016) 337.
[50] R. Zhang, H. Alamdari, S. Kaliaguine, Appl. Catal. A 340 (2008) 140.
[51] R. Zhang, A. Villanueva, H. Alamdari, S. Kaliaguine, J. Catal. 237 (2006) 368.
[52] M.M. Nair, H. Yen, F. Kleitz, C. R. Chim. 17 (2014) 641–655.
[53] H. Yen, Y. Seo, R. Guillet-Nicolas, S. Kaliaguine, F. Kleitz, Chem. Commun. (Cambridge U. K.) 47 (2011) 10473.
[54] H. Yen, Y. Seo, S. Kaliaguine, F. Kleitz, Angew. Chem. Int. Ed. 51 (2012) 12032.
[55] H.-B. Zhang, X. Dong, G.-D. Lin, X.-L. Liang, H.-Y. Li, Chem. Commun. (Cambridge U. K.) 0 (2005) 5094.
[56] J.E. Baker, R. Burch, S.J. Hibble, P.K. Loader, Appl. Catal. 65 (1990) 281.
[57] A.F. Cunha, J.J.M. Órfão, J.L. Figueiredo, Fuel Process. Technol. 90 (2009) 1234.
[58] D.M. Minahan, W.M. Hart, W. Epling, G. Hoflund, Synthesis of Fuel Alcohols and MTBE from Syngas Using Spinel Oxide Based Catalysts, (1997) p. 715.
[59] J.C. Slaa, J.G. van Ommen, J.R.H. Ross, Catal. Today 15 (1992) 129.
[60] Y. Liu, K. Murata, M. Inaba, I. Takahara, K. Okabe, Fuel 104 (2013) 62.
[61] M.N. Ha, G. Lu, Z. Liu, L. Wang, Z. Zhao, J. Mater. Chem. A 4 (2016) 13155.